

Quantitative determination of modal photon number density spectrum in arbitrary dielectric structures with a quantum emitter

Li-Heng Chen(陈立恒)†, Fengfeng Luo(罗凤凤), and Yonggui Gao(高勇贵)

Citation: Chin. Phys. B, 2025, 34 (**4**): 044204. DOI: 10.1088/1674-1056/adb262
Journal homepage: http://cpb.iphy.ac.cn; http://iopscience.iop.org/cpb

What follows is a list of articles you may be interested in

Topological transmission and topological corner states combiner in all-dielectric honeycomb valley photonic crystals

Ming Sun(孙铭), Xiao-Fang Xu(许孝芳), Yun-Feng Shen(沈云峰), Ya-Qing Chang(常雅箐), and Wen-Ji Zhou(周文佶)
Chin. Phys. B, 2025, 34 (**3**): 034206. DOI: 10.1088/1674-1056/ada9d9

Topological edge and corner states of valley photonic crystals with zipper-like boundary conditions

Yun-Feng Shen(沈云峰), Xiao-Fang Xu(许孝芳), Ming Sun(孙铭), Wen-Ji Zhou(周文佶), and Ya-Jing Chang(常雅箐)
Chin. Phys. B, 2024, 33 (**4**): 044203. DOI: 10.1088/1674-1056/ad1e6a

High-performance chiral all-optical OR logic gate based on topological edge states of valley photonic crystal

Xiaorong Wang(王晓蓉), Hongming Fei(费宏明), Han Lin(林瀚), Min Wu(武敏), Lijuan Kang(康丽娟), Mingda Zhang(张明达), Xin Liu(刘欣), Yibiao Yang(杨毅彪), and Liantuan Xiao(肖连团)
Chin. Phys. B, 2023, 32 (**7**): 074205. DOI: 10.1088/1674-1056/accb41

Grain boundary effect on structural, optical, and electrical properties of sol-gel synthesized Fe-doped SnO_2 nanoparticles

Archana V, Lakshmi Mohan, Kathirvel P, and Saravanakumar S
Chin. Phys. B, 2021, 30 (**4**): 048202. DOI: 10.1088/1674-1056/abc2c1

Structural, vibrational, optical, photoluminescence, thermal, dielectric, and mechanical studies on zinc (tris) thiourea sulfate single crystal: A noticeable effect of organic dye

Mohd Shkir, V Ganesh, S AlFaify, I S Yahia, Mohd Anis
Chin. Phys. B, 2018, 27 (**5**): 054216. DOI: 10.1088/1674-1056/27/5/054216

Quantitative determination of modal photon number density spectrum in arbitrary dielectric structures with a quantum emitter

Li-Heng Chen(陈立恒)[†], Fengfeng Luo(罗凤凤), and Yonggui Gao(高勇贵)

Department of Basic Courses Teaching, Software Engineering Institute of Guangzhou, Guangzhou 510990, *China*

(Received 7 November 2024; revised manuscript received 19 January 2025; accepted manuscript online 5 February 2025)

Understanding the photon number statistics of a quantum emitter (QE) interacting with complex photonic environments is fundamental to advances in quantum optics and nanophotonics. We introduce a general theoretical framework for calculating the modal photon number density spectrum (MPNDS) in arbitrary dielectric structures with an embedded two-level QE. We validate our approach by investigating a system composed of a two-level QE and a photonic crystal (PhC) slab with an L3 cavity and a waveguide, finding that the MPNDS exhibits significant changes in both waveguide and background radiative channels as the interaction between the QE and modal field transitions from weak coupling to strong coupling. We observe that the number of photons guided along the waveguide shows a strong dependence on the QE's transition frequency and transition dipole moment, but demonstrates robustness to the transition dipole moment when the transition frequency approaches the waveguide cutoff frequency. Our work allows for the determination and tailoring of light emission characteristics across diverse radiative channels in complex photonic environments.

Keywords: beta factor, light extraction efficiency, photoluminescence spectrum, photonic crystals, power spectrum, spontaneous emission, strong coupling interaction

PACS: 42.50.Pq, 42.50.Ct, 42.70.Qs

DOI: 10.1088/1674-1056/adb262 **CSTR:** 32038.14.CPB.adb262

1. Introduction

Light–matter interaction at the quantum level is a fundamental aspect of quantum physics, playing a crucial role in the development of novel quantum technologies. Among these interactions, the coupling of the quantum emitters (QEs) with their photonic environment has garnered significant attention due to its potential applications in quantum optics and nanophotonics.[1–3] A diverse range of QEs is being actively investigated, spanning from quantum dots,[2,4–17] nitrogen-vacancy centers,[18–20] monolayer tungsten diselenide,[21] carbon nanotubes,[22] graphene,[23] black phosphorus[24] and DNA origami.[25] These advancements are paving the way for applications such as single-photon sources,[4,10,14,26] strong coupling[5,8,11,12] and radiative coupling,[6,15,27,28] which are essential for enabling quantum communication and quantum information processing.[16,17]

Probing and analyzing the photons emitted from quantum systems reveal insights into their underlying physics and dynamics. The widely used metric is the power spectrum, defined as $S\left(\boldsymbol{r}_{\mathrm{p}},\omega\right)=\int_0^\infty \mathrm{d}t_2\int_0^\infty \mathrm{d}t_1\,\mathrm{e}^{-\mathrm{i}\omega(t_2-t_1)}\langle \boldsymbol{E}^{(-)}\left(\boldsymbol{r}_{\mathrm{p}},t_2\right)\cdot\boldsymbol{E}^{(+)}\left(\boldsymbol{r}_{\mathrm{p}},t_1\right)\rangle$,[29–31] providing a spatially resolved picture of the emitted light intensity, which is proportional to the spectrum measured by a photodetector at a specific point $\boldsymbol{r}_{\mathrm{p}}$ and closely relates to photoluminescence spectra measured in experiments. However, its inherent spatial dependence limits its ability to quantify the photon number in a specific mode set. Another widely used metric is the beta factor, defined as $\Gamma_{\mathrm{m}}/\Gamma$,[7,13] where Γ_{m} represents the decay rate of the QE into a specific mode and Γ is its total decay rate. Thus, the beta factor represents the probability of a single QE emitting a single photon into a specific mode. However, its applicability is restricted to the weak coupling regime and is not suitable for strong coupling or more generalized interactions. Thus, accurately quantifying the number of photons emitted by a QE through a specific mode set in a complex photonic environment remains challenging.

The limitations outlined above motivated us to introduce the modal photon number density spectrum (MPNDS) in this paper, which directly connects to the spectrum measured by a spectrometer positioned in the corresponding radiative channel. We present a comprehensive theoretical framework for quantitatively calculating the MPNDS of a system composed of a single two-level QE and an arbitrary dielectric structure. Our findings reveal that the MPNDS strongly depends on both the QE's evolution spectrum and the modal projected local density of states (PLDOS), reflecting the combined influence of the QE and the photonic environment. Moreover, the MPNDS determines the photon number in a specific mode set, enabling investigations into photon extraction efficiency and related phenomena in various nanophotonic systems. We validate our approach by investigating a system composed of a QE and a photonic crystal (PhC) slab[32] with an L3 cavity[33–35] and a waveguide,[7,9,13] demonstrating that the calculated MP-

[†]Corresponding author. E-mail: chlheng@qq.com

© 2025 Chinese Physical Society and IOP Publishing Ltd. All rights, including for text and data mining, AI training, and similar technologies, are reserved.

NDS accurately reflects the photon emission behavior of the coupled system. Notably, we observe a substantial impact on the MPNDS of the waveguide and background radiative channels as the interaction between the QE and the photonic environment changes from weak to strong coupling. Furthermore, we investigate the functional dependence of the photon number propagating along the waveguide on the QE's transition frequency and transition dipole moment. We find that the monotonic relationship between photon number and transition dipole moment reverses as the transition frequency crosses the waveguide cutoff frequency. Near this crossover, the photon number demonstrates robustness against variations in the transition dipole moment. Our work allows for the determination and tailoring of the light emission properties in different radiative channels, providing a powerful tool for understanding and optimizing light–matter interactions in complex photonic environments.

2. Method

The interaction between a two-level QE and the electromagnetic field modulated by a dielectric structure can be described using the electric dipole approximation and rotating wave approximation, with the Hamiltonian given by[36,37]

$$\begin{aligned} H &= \sum_{\lambda} \hbar\omega_{\lambda} a_{\lambda}^{\dagger} a_{\lambda} + \hbar\omega_0 \sigma_+ \sigma_- \\ &\quad + \hbar \sum_{\lambda} \left[g_{\lambda} \sigma_+ a_{\lambda} + g_{\lambda}^* a_{\lambda}^{\dagger} \sigma_- \right], \end{aligned} \tag{1}$$

where ω_0 is the transition frequency between the excited state $|e\rangle$ and the ground state $|g\rangle$ of the QE. The lowering and raising operators of the QE are given by $\sigma_- = |g\rangle\langle e|$ and $\sigma_+ = |e\rangle\langle g|$, respectively. The modal field is labeled as λ. ω_λ, $a_\lambda^\dagger$ and a_λ are the eigenfrequency, creation operator and annihilation operator of the modal field $\boldsymbol{E}_\lambda(\boldsymbol{r})$ of the dielectric structure, respectively. The $\boldsymbol{E}_\lambda(\boldsymbol{r})$ satisfies the Helmholtz equation, $\nabla \times \nabla \times \boldsymbol{E}_\lambda(\boldsymbol{r}) - (\omega_\lambda/c)^2 \varepsilon(\boldsymbol{r}) \boldsymbol{E}_\lambda(\boldsymbol{r}) = \boldsymbol{0}$, and the orthonormal relation, $\int_V \varepsilon(\boldsymbol{r}) \boldsymbol{E}_\lambda^*(\boldsymbol{r}) \cdot \boldsymbol{E}_{\lambda'}(\boldsymbol{r}) \, \mathrm{d}\boldsymbol{r} = \delta_{\lambda,\lambda'}$, where $\varepsilon(\boldsymbol{r})$ is the relative permittivity of the dielectric. The coupling coefficient between the QE and mode λ is given by $g_\lambda = -\mathrm{i}\omega_0 (2\varepsilon_0 \hbar \omega_\lambda)^{-1/2} \boldsymbol{E}_\lambda(\boldsymbol{r}_0) \cdot \boldsymbol{d}_0$, where $\boldsymbol{d}_0$ is the transition dipole moment of the QE located at $\boldsymbol{r}_0$. Furthermore, g_λ exhibits a dependence on the modal volume V_λ of mode λ, with a scaling of $g_\lambda \sim V_\lambda^{-1/2}$, see Appendix A1. The Hamiltonian presented in Eq. (1) is compatible with that derived from coupled-mode theory (CMT), see Appendix A2. The state vector at time t can be expressed as

$$|\Psi(t)\rangle = C_e(t) |e, \{0\}\rangle + \sum_{\lambda} C_{g\lambda}(t) |g, \{1_\lambda\}\rangle, \tag{2}$$

where $|e, \{0\}\rangle$ is the direct product of the QE excited state and the photon vacuum state, while $|g, \{1_\lambda\}\rangle$ is the direct product of the QE ground state and the single-photon state of mode λ. We assume that the QE is initially prepared in excited state, with $C_e(0) = 1$, and the rest of the system is in vacuum, with $C_{g\lambda}(0) = 0$ for any mode λ. Substituting Eqs. (1) and (2) into the Schrödinger equation yields the evolution dynamics as

$$C_{g\lambda}(t) = \mathrm{e}^{-\mathrm{i}\omega_\lambda t} \left(-\mathrm{i} g_\lambda^*\right) \int_0^t C_e(t') \, \mathrm{e}^{\mathrm{i}\omega_\lambda t'} \, \mathrm{d}t'. \tag{3}$$

As the system evolves over time, specifically when $t \to \infty$, the integral $\int_0^t C_e(t') \, \mathrm{e}^{\mathrm{i}\omega_\lambda t'} \, \mathrm{d}t'$ approaches the forward Laplace transform of $C_e(t)$, denoted as $\bar{C}_e(\omega_\lambda)$. Thus,

$$C_{g\lambda}(t)\big|_{t\to\infty} = \mathrm{e}^{-\mathrm{i}\omega_\lambda t} \left(-\mathrm{i} g_\lambda^*\right) \bar{C}_e(\omega_\lambda). \tag{4}$$

To investigate the photon number of specific mode set, we define the modal photon number as

$$N_S = \langle \Psi(t) | \sum_{\lambda \in S} a_\lambda^\dagger a_\lambda \, |\Psi(t)\rangle \Big|_{t\to\infty} = \sum_{\lambda \in S} \left| C_{g\lambda}(t) \right|^2 \Big|_{t\to\infty}, \tag{5}$$

where S represents the set of specific modes under investigation. N_S is the value measured by a photon counter positioned in the radiative channel corresponding to the mode set S. To facilitate numerical calculations, we introduce the modal PLDOS, $\rho_S(\omega)$, and the modal local coupling strength of the mode set S, $\Gamma_S(\omega)$, defined as

$$\rho_S(\omega) = \sum_{\lambda \in S} \left| \boldsymbol{E}_\lambda(\boldsymbol{r}_0) \cdot \hat{d}_0 \right|^2 \delta(\omega - \omega_\lambda), \tag{6}$$

$$\Gamma_S(\omega) = 2\pi \sum_{\lambda \in S} |g_\lambda|^2 \, \delta(\omega - \omega_\lambda), \tag{7}$$

where $\hat{d}_0 = \boldsymbol{d}_0/|\boldsymbol{d}_0|$ is the directional vector of $\boldsymbol{d}_0$. These definitions align with previous works[38] but restrict summation to the mode set S, instead of the universal set S_{all} which contains all modes. The relationship between $\rho_S(\omega)$ and $\Gamma_S(\omega)$ can be established as (see Appendix A3)

$$\Gamma_S(\omega) = \Gamma_0 \frac{\omega}{\omega_0} M_S(\omega), \tag{8}$$

where $\Gamma_0 = \omega_0^3 d_0^2/(3\pi\hbar\varepsilon_0 c^3)$ is the spontaneous emission rate of the QE in vacuum,[29] and $M_S(\omega) = \rho_S(\omega)/\rho_0(\omega)$ is the multiplication factor (M factor) of the mode set S, with $\rho_0(\omega) = \omega^2/(3\pi^2 c^3)$ representing the PLDOS in vacuum.[29] $M_S(\omega)$ can be calculated by normalizing the power radiated by a dipole to the mode set S against its radiated power in vacuum, see Appendix A4. Considering Eq. (5) and utilizing Eqs. (4) and (7), we find that N_S can be expressed as

$$\begin{aligned} N_S &= \int_{-\infty}^{+\infty} \sum_{\lambda \in S} \left| C_{g\lambda}(t) \right|^2 \Big|_{t\to\infty} \delta(\omega - \omega_\lambda) \, \mathrm{d}\omega \\ &= \int_{-\infty}^{+\infty} \left| \bar{C}_e(\omega) \right|^2 \sum_{\lambda \in S} |g_\lambda|^2 \, \delta(\omega - \omega_\lambda) \, \mathrm{d}\omega \\ &= \frac{1}{2\pi} \int_{-\infty}^{+\infty} \Gamma_S(\omega) \left| \bar{C}_e(\omega) \right|^2 \mathrm{d}\omega. \end{aligned} \tag{9}$$

Using Eq. (8), N_S can also be written as

$$N_S = \frac{1}{2\pi}\int_{-\infty}^{+\infty} \Gamma_0 \frac{\omega}{\omega_0} M_S(\omega)\left|\bar{C}_e(\omega)\right|^2 \mathrm{d}\omega. \tag{10}$$

Note that $N_{S_{\text{all}}} = 1$ since the two-level QE emits one photon when the system reaches a steady state. Therefore, N_S can also be interpreted as the photon extraction efficiency of the mode set S. Additionally, according to the integrand in Eq. (10), we define

$$T_S(\omega) = \Gamma_0 \frac{\omega}{\omega_0} M_S(\omega)\left|\bar{C}_e(\omega)\right|^2 \tag{11}$$

as the MPNDS of the mode set S. From Eqs. (10) and (11), we obtain $N_S = \frac{1}{2\pi}\int_{-\infty}^{+\infty} T_S(\omega)\,\mathrm{d}\omega$, therefore, $T_S(\omega)$ can be interpreted as the photon number density of the mode set S at frequency ω.

The power spectrum can be expressed as $S(\boldsymbol{r}_\mathrm{p},\omega) = \frac{\omega^2}{\varepsilon_0 c^2}\left|\boldsymbol{G}(\boldsymbol{r}_\mathrm{p},\boldsymbol{r}_0,\omega)\cdot\boldsymbol{d}\right|\left|\bar{C}_e(\omega)\right|^2$, see Appendix A5. Comparing this with Eq. (11), it is evident that the power spectrum and the MPNDS share the common factor $\left|\bar{C}_e(\omega)\right|^2$. Moreover, the Green's function, $\boldsymbol{G}(\boldsymbol{r}_\mathrm{p},\boldsymbol{r}_0,\omega)$, and the M factor for mode set S, $M_S(\omega)$, are determined solely by the dielectric's properties. Therefore, both the power spectrum and the MPNDS reflect the overall properties of the dielectric system and the QE. However, a key distinction arises in their dependence. The power spectrum, $S(\boldsymbol{r}_\mathrm{p},\omega)$, is $\boldsymbol{r}_\mathrm{p}$-dependent, and generally varies spatially. For an atom with an infinite number of energy levels located at $\boldsymbol{r}_\mathrm{p}$, where the modal field is linearly polarized, $S(\boldsymbol{r}_\mathrm{p},\omega)$ is proportional to the probability of the atom transitioning from its ground state to an excited state with an energy difference of $\hbar\omega$.[29] This clearly demonstrates that the power spectrum does not represent a photon number density spectrum. Indeed, defining the photon number at a specific point $\boldsymbol{r}_\mathrm{p}$ is physically problematic. In contrast, the MPNDS, $T_S(\omega)$, depends on the mode set S. Since the modal fields inherently possess a spatial distribution, the MPNDS cannot be solely dependent on a single point. $T_S(\omega)$ represents the spectrum measured by a spectrometer positioned in the radiative channel corresponding to the mode set S. A similar discussion can be applied to the modal photon number N_S according to Eq. (10).

Considering disjoint sets $S_i \cap S_j = \emptyset$ for any i and j, with $S_{\text{all}} = \bigcup_i S_i$, it is straightforward to verify that

$$M_{S_{\text{all}}}(\omega) = \sum_i M_{S_i}(\omega), \tag{12}$$

$$N_{S_{\text{all}}} = \sum_i N_{S_i}, \tag{13}$$

$$T_{S_{\text{all}}}(\omega) = \sum_i T_{S_i}(\omega). \tag{14}$$

In summary, we have derived the expressions for the MPNDS valid for any system composed of a two-level QE and an arbitrary dielectric structure. To facilitate numerical calculations, we outline the following steps: first, numerically calculate the M factor $M_{S_{\text{all}}}(\omega)$ or Green's function $\boldsymbol{G}(\boldsymbol{r},\boldsymbol{r}_0,\omega)$ for a dipole at position $\boldsymbol{r}_0$ oriented in the direction of $\boldsymbol{d}_0$; second, use local coupling theory to obtain the QE's evolution spectrum $\bar{C}_e(\omega)$ from the calculated M factor or Green's function;[38] third, specify the mode set S under investigation and numerically calculate the power radiated into this mode set to obtain the modal M factor $M_S(\omega)$; finally, use Eqs. (11) and (10) to obtain the MPNDS, $T_S(\omega)$, and the modal photon number N_S. These steps are straightforward and suitable for practical numerical calculations. Our numerical method will serve as a powerful tool for investigating a wide range of light–matter interactions.

3. Result and discussion

As an application of our method, we focus on a system composed of a QE and a PhC slab with an L3 cavity and a waveguide. Our model structure, shown in Fig. 1(a), consists of a line defect along the x direction in a two-dimensional triangular air-hole dielectric PhC slab with a lattice constant of $a = 400$ nm. The distance between the centers of the nearest-neighbor holes on either side of the waveguide is $\sqrt{3}a$. The background is a vacuum, while the slab material is silicon with a refractive index of $n = 3.46$. The slab thickness is set to $d = 0.55a$, while the air-hole radius is $r = 0.25a$. A finely optimized L3 cavity is placed at a distance of $6a$ from the central axis of the waveguide. From inside to outside, the air holes marked with arrows are shifted outwards by $0.337a$, $0.270a$, $0.088a$, $0.323a$ and $0.173a$, respectively, to improve the quality factor of the bare cavity to 4.2×10^6.[34] The radii of the air holes adjacent to the waveguide (enclosed in red rectangles) are increased by 5.84 nm to increase the cutoff frequency f_{cut}. A two-level QE, polarized along the y direction, is located at the central point $\boldsymbol{r}_0$ of the cavity, as indicated by $\hat{d}_0$ and an upward arrow at the center of the L3 cavity. We assume that the QE is initially prepared in the excited state, with $C_e(0) = 1$, and the rest of the system is in the vacuum state, with $C_{g\lambda}(0) = 0$ for any mode λ. The photon emitted from the QE can propagate through two radiative channels: the waveguide and the background above and below the PhC slab. The waveguide supports a set of Bloch modes, denoted by S_{WG}, while the background supports a set of leakage modes, denoted by S_{BG}.

We use the finite-difference time-domain method[39] for simulations, with a dipole excitation source matching the QE's position and polarization. Our goal is to calculate the MPNDS for both the waveguide channel S_{WG} and background channel S_{BG}, represented by $T_{S_{\text{WG}}}(\omega)$ and $T_{S_{\text{BG}}}(\omega)$, respectively, using Eq. (11). This requires the determination of the QE's evolution spectrum $\left|\bar{C}_e(\omega)\right|^2$, as well as the M factors

$M_{S_{\rm WG}}(\omega)$ and $M_{S_{\rm BG}}(\omega)$. According to local coupling theory, $\left|\bar{C}_e(\omega)\right|^2$ can be obtained from $M_{S_{\rm all}}(\omega)$, which is calculated from the radiated power of the dipole numerically. To calculate $M_{S_{\rm WG}}(\omega)$, two cross sections are placed on either side of the waveguide to record the radiated power passing through them. These cross sections are located far away from $\boldsymbol{r}_0$ in the x direction (up to $30a$) to minimize near-field influence. Because $S_{\rm all} = S_{\rm WG} \cup S_{\rm BG}$ and $S_{\rm WG} \cap S_{\rm BG} = \emptyset$, equation (12) demonstrates that $M_{S_{\rm BG}}(\omega)$ can be determined from the known $M_{S_{\rm all}}(\omega)$ and $M_{S_{\rm WG}}(\omega)$. Finally, using Eq. (11), we can determine $T_{S_{\rm BG}}(\omega)$ from the obtained $M_{S_{\rm BG}}(\omega)$.

The electromagnetic field propagating along the waveguide exhibits strong dispersion characteristics near its cutoff frequency $f_{\rm cut}$, which can lead to significant reflections within the perfectly matched layer (PML). To minimize these reflections, we implemented 2100 layers of PML from $x = 30a$ to $x = 135a$, with small parameters related to the absorption strength to ensure a smooth decay of the electromagnetic field within the PML. We also adjusted the air holes on both sides of the waveguide in the third row. Specifically, from $x = 30a$ to $x = 135a$, each subsequent air-hole radius is reduced by 0.1143 nm. This gradual reduction ensures that the cutoff frequencies $f'_{\rm cut}$ of the waveguide within the PML decrease gradually with x, thereby moving $f'_{\rm cut}$ further away from the frequency of the electromagnetic field and, thus, weakening both the dispersion effect and reflection. These adjustments were symmetrically applied to the air holes from $x = -30a$ to $x = -135a$.

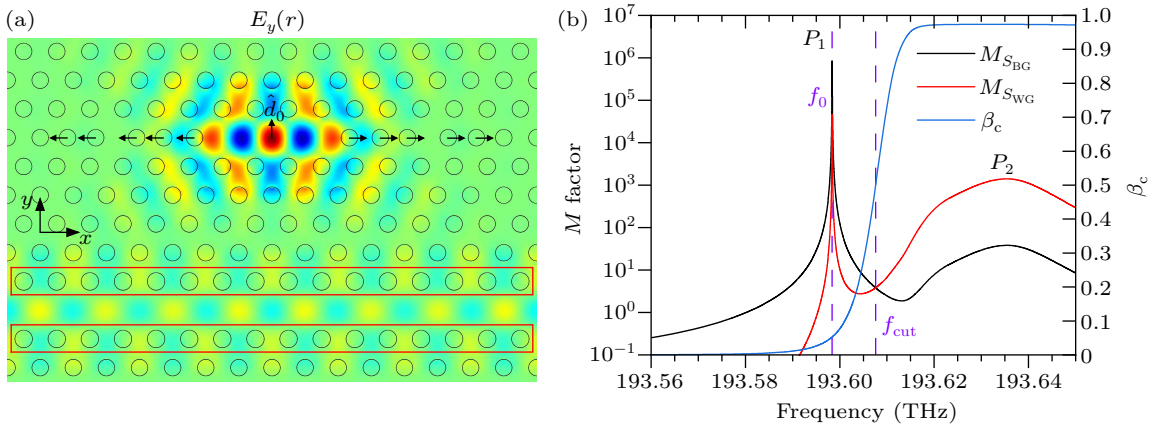


Fig. 1. Hybrid system composed of a QE and a PhC slab with an L3 cavity and a waveguide. (a) $E_y(\boldsymbol{r})$ component of the electric modal field. Black circles denote air holes. The air holes marked with arrows on both sides of the L3 cavity are shifted outward. The radii of the nearest-neighbor holes within the red rectangles on either side of the waveguide are increased. A QE polarized along $\hat{d}_0$ indicated by an upward arrow is positioned at the center of the L3 cavity. (b) M factor of the mode sets $S_{\rm BG}$ (black line), $S_{\rm WG}$ (red line) and beta factor $\beta_{\rm c}$ (blue line), respectively. The purple dashed lines represent the QE's transition frequency f_0 and waveguide cutoff frequency $f_{\rm cut}$, respectively. The peaks of the M factor spectra are labeled as P_1 and P_2, respectively. The electric modal field in (a) corresponds to the peak P_1.

We define the beta factor $\beta_{\rm c}(\omega)$ as $M_{S_{\rm WG}}(\omega)/M_{S_{\rm all}}(\omega)$, which serves as a metric for the classical light extraction efficiency into the waveguide. Figure 1(b) illustrates the M-factor and beta-factor spectra. At lower frequencies, the beta factor approaches zero, indicating that the electromagnetic field in this frequency range cannot propagate along the waveguide, thus suppressing $M_{S_{\rm WG}}(\omega)$. Due to the resonant frequency of the cavity-waveguide coupled mode shown in Fig. 1(a) lying within this frequency range, the modal field is long confined in the high-quality-factor L3 cavity and leaks slowly into the background. This results in a prominent, sharp peak P_1 in $M_{S_{\rm BG}}(\omega)$, with a frequency of 193.5984 THz and a quality factor of 4.89×10^6. As the frequency increases, the beta factor rapidly approaches one, implying that the electromagnetic field in this frequency range can efficiently couple into the waveguide and propagate with minimal leakage into the background, leading to a shallow, broad peak P_2 in $M_{S_{\rm WG}}(\omega)$ and suppression of $M_{S_{\rm BG}}(\omega)$. As mentioned, we have adjusted the air holes around the waveguide, thereby breaking its translational symmetry along the x direction. Consequently, the cutoff frequency $f_{\rm cut}$ loses its strict meaning. For convenience in subsequent discussions, we define $f_{\rm cut}$ as the frequency at which the beta factor is 0.5, i.e., $f_{\rm cut} = 193.6076$ THz, indicated by the purple dashed line in Fig. 1(b).

From these numerical results, the relative magnitudes of $M_{S_{\rm WG}}(\omega)$ and $M_{S_{\rm BG}}(\omega)$ dramatically invert across the cutoff frequency. Based on Eqs. (10) and (11), the distribution of $\left|\bar{C}_e(\omega)\right|^2$ relative to $f_{\rm cut}$ dictates the photon's propagation path. If $\left|\bar{C}_e(\omega)\right|^2$ lies primarily below $f_{\rm cut}$, the photon predominantly occupies the $S_{\rm BG}$ mode set, propagating mainly within the background due to significant overlap with $M_{S_{\rm BG}}(\omega)$ and minimal overlap with $M_{S_{\rm WG}}(\omega)$. Conversely, if $\left|\bar{C}_e(\omega)\right|^2$ extends across $f_{\rm cut}$, the photon distributes comparably between the $S_{\rm WG}$ and the $S_{\rm BG}$ mode sets, resulting in propagation through both the waveguide and the background, as the overlap with both $M_{S_{\rm WG}}(\omega)$ and $M_{S_{\rm BG}}(\omega)$ is similar. To achieve these two distinct evolution spectra, we adjust the QE's transition dipole moment d_0, which is equivalent to ad-

justing its lifetime τ_0 in vacuum since $\tau_0 = 3\pi\hbar\varepsilon_0 c^3/(\omega_0^3 d_0^2)$ holds.[29] This controls the coupling strength between the QE and the photonic environment, thereby realizing weak and strong coupling interactions. In the weak coupling regime, the QE spontaneously decays from its excited state to the ground state, emitting a photon. The population of the excited state $|C_e(t)|^2$ decays monotonically over time, exhibiting a single-peak structure in the QE's evolution spectrum $|\bar{C}_e(\omega)|^2$. In the strong coupling regime, the QE repeatedly emits and absorbs photons, leading to an oscillatory process in $|C_e(t)|^2$, known as vacuum Rabi oscillation. This manifests as a double-peak structure in $|\bar{C}_e(\omega)|^2$, known as vacuum Rabi splitting. By carefully selecting the appropriate transition frequency of the QE, we can tailor $|\bar{C}_e(\omega)|^2$ to primarily distribute below f_{cut} under weak coupling and simultaneously extend across f_{cut} under strong coupling. This enables control over the MPNDS and photon numbers in both the waveguide and background radiative channels.

Initially, we set the transition frequency of the QE to that of the peak P_1 in Fig. 1(b), i.e., $f_0 = 193.5984$ THz, indicated by the purple dashed line. The QE's lifetime in vacuum is set to $\tau_0 = 150$ ns. Here, τ_0 can be interpreted as an effective lifetime, which can be adjusted by varying the angle between the QE's transition dipole moment and $\boldsymbol{E}(\boldsymbol{r}_0)$, see Appendix A6. As shown in Fig. 2(a), although a double-peak structure is presented in $|\bar{C}_e(\omega)|^2$, the peak P_1 is clearly dominant. The inset shows that $|C_e(t)|^2$ decreases monotonically over time, indicating that the QE mainly evolves under weak coupling. Comparing Figs. 1(b) and 2(a) reveals that $|\bar{C}_e(\omega)|^2$ overlaps minimally with $M_{S_{\text{WG}}}(\omega)$ but significantly with $M_{S_{\text{BG}}}(\omega)$. This leads to a small MPNDS of the waveguide, $T_{S_{\text{WG}}}(\omega)$, and a large MPNDS of the background, $T_{S_{\text{BG}}}(\omega)$, as shown in Fig. 2(b). According to Eq. (11), the number of photons propagating along the waveguide and the background, $N_{S_{\text{WG}}}$ and $N_{S_{\text{BG}}}$, are calculated to be 5.59×10^{-3} and 0.994, respectively. These results demonstrate that photons can hardly propagate along the waveguide but rather through the background.

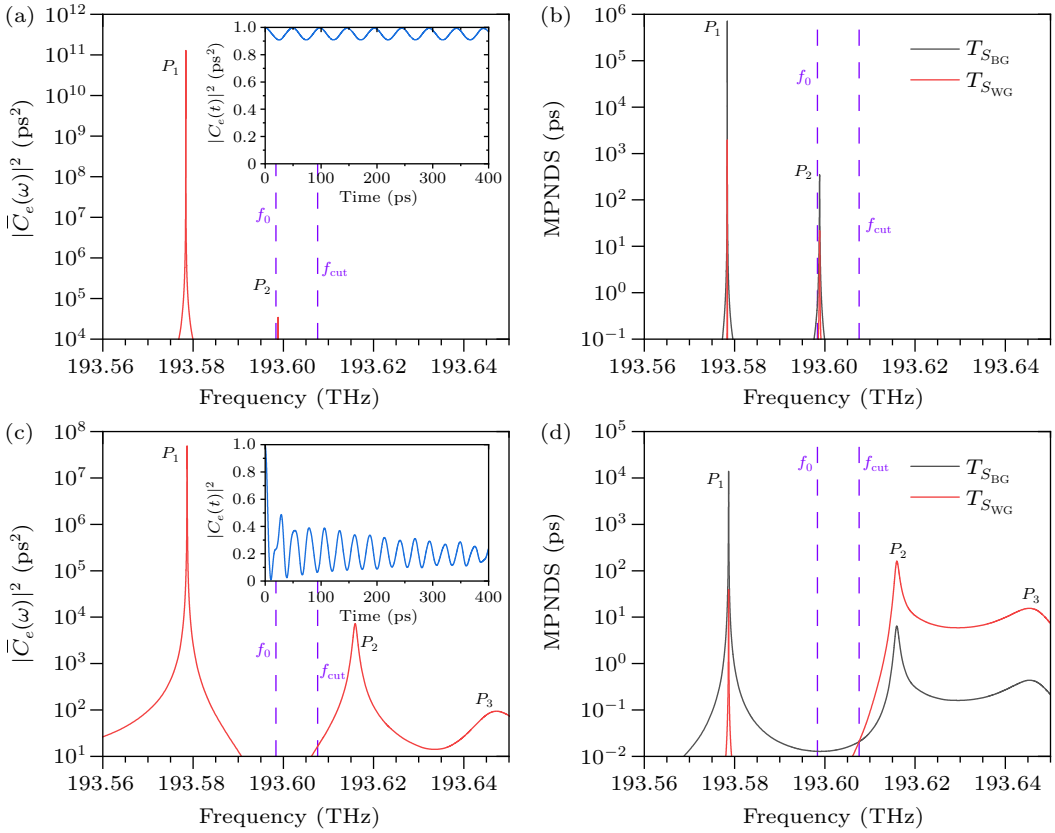


Fig. 2. Evolution spectra and dynamics of the coupled system. [(a), (c)] Evolution spectra $|\bar{C}_e(\omega)|^2$ and the population of excited state $|C_e(t)|^2$ (insets) of the QE in the weak (a) and strong (c) coupling regimes, respectively. [(b), (d)] The MPNDS of the mode sets S_{BG} (black line) and S_{WG} (red line) in the weak (b) and strong (d) coupling regimes, respectively. The purple dashed lines represent the QE's transition frequency f_0 and waveguide cutoff frequency f_{cut}, respectively. The peaks are labeled as P_1, P_2 and P_3, respectively.

Next, we reduce the lifetime of the QE in vacuum to $\tau_0 = 3$ ns while keeping the transition frequency f_0 fixed. In the frequency range shown in Fig. 2(c), a triple-peak structure appears in $|\bar{C}_e(\omega)|^2$, denoted as P_1, P_2 and P_3 from low to high frequency, respectively. Notably, the P_1 peak lies below f_{cut}, enabling its corresponding photons to be long confined within the high-quality-factor L3 cavity. Consequently, the P_1 peak exhibits a prominent, narrow line shape. Conversely, the P_2 and P_3 peaks exceed f_{cut}, allowing their corresponding photons to efficiently couple into and propagate

along the waveguide, resulting in a shallow, broad line shape. The inset shows that $|C_e(t)|^2$ undergoes an oscillatory process, indicating that the QE mainly evolves under strong coupling. Comparing Figs. 1(b) and 2(c) reveals that below the cutoff frequency, $|\bar{C}_e(\omega)|^2$ overlaps less with $M_{S_{\rm WG}}(\omega)$ and more with $M_{S_{\rm BG}}(\omega)$, leading to smaller $T_{S_{\rm WG}}(\omega)$ than $T_{S_{\rm BG}}(\omega)$. Above the cutoff frequency, $|\bar{C}_e(\omega)|^2$ overlaps more with $M_{S_{\rm WG}}(\omega)$ and less with $M_{S_{\rm BG}}(\omega)$, leading to larger $T_{S_{\rm WG}}(\omega)$ than $T_{S_{\rm BG}}(\omega)$, as shown in Fig. 2(d). From Eq. (10), we obtain $N_{S_{\rm WG}} = 0.543$ and $N_{S_{\rm BG}} = 0.457$, respectively. These findings suggest that photons can propagate both along the waveguide and through the background, with comparable probabilities.

To further investigate how the QE's dynamics influence photon propagation along the waveguide, we varied the QE's transition frequency, f_0, from 193.578 THz to 193.618 THz, and its vacuum lifetime, τ_0, from 3 ns to 150 ns. We calculated $N_{S_{\rm WG}}$ as a function of f_0 and τ_0, denoted by $N_{S_{\rm WG}}(f_0,\tau_0)$, using Eq. (10). The numerical values and contour lines of $N_{S_{\rm WG}}$ are shown in Fig. 3. For any given τ_0, $N_{S_{\rm WG}}$ increases monotonically with f_0. Especially, as f_0 approaches $f_{\rm cut}$, the contour lines become denser, signifying a sharp increase in $N_{S_{\rm WG}}$. This is attributed to the substantial increase in overlap between $|\bar{C}_e(\omega)|^2$ and $M_{S_{\rm WG}}(\omega)$. Additionally, for a given f_0, if f_0 is around or below $f_{\rm cut}$, $N_{S_{\rm WG}}$ decreases monotonically with τ_0, consistent with our discussion in Fig. 2. However, if f_0 is around or above $f_{\rm cut}$, the situation is reversed, and $N_{S_{\rm WG}}$ increases monotonically with τ_0, except for small τ_0. This is because as τ_0 decreases, the increased coupling strength leads to a larger Rabi splitting. The peak in $|\bar{C}_e(\omega)|^2$ with frequency lower than f_0 is redshifted, bringing its frequency closer to or even below $f_{\rm cut}$. Consequently, the overlap between $|\bar{C}_e(\omega)|^2$ and $M_{S_{\rm WG}}(\omega)$ decreases, resulting in a lower $N_{S_{\rm WG}}$. The opposing monotonicity of $N_{S_{\rm WG}}$ with respect to τ_0 on either side of $f_{\rm cut}$ leads to an invariant behavior for $N_{S_{\rm WG}}$ near $f_{\rm cut}$. As shown by the contour lines, when $f_0 \approx 193.611$ THz, $N_{S_{\rm WG}}$ is nearly stable at 0.8, except for small τ_0, demonstrating robustness against variations in the QE's transition dipole moment.

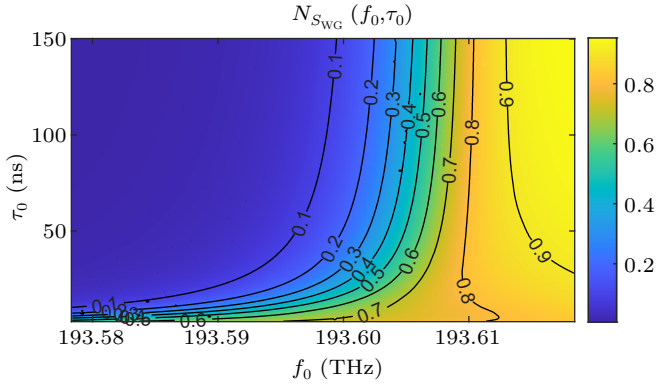


Fig. 3. Photon number of the mode set $S_{\rm WG}$, $N_{S_{\rm WG}}$, as a function of the QE's transition frequency f_0 and lifetime in vacuum τ_0. Black curves are contour lines of $N_{S_{\rm WG}}$.

4. Conclusion

This work presents a comprehensive theoretical framework for quantitatively calculating the MPNDS of a system composed of a single two-level QE and an arbitrary dielectric structure. We find that the MPNDS is determined by the modal PLDOS and the QE's evolution spectrum, both of which can be calculated using established methods. The versatility of this framework is demonstrated through its successful application to a PhC slab system featuring an L3 cavity and waveguide coupled to a QE. Our results reveal that the MPNDS strongly depends on the QE's transition frequency and transition dipole moment. By adjusting the QE's transition dipole moment, we demonstrated control over the photon propagation: when the QE's transition frequency lies below the cutoff frequency, weak coupling favors background propagation, while strong coupling enables bidirectional propagation along both waveguide and background channels. We find that the monotonic relationship between photon number and transition dipole moment is reversed as the transition frequency crosses the waveguide cutoff frequency. Near this crossover, the photon number exhibits robustness against variations in the transition dipole moment. Future work will address the robustness of the integrated power spectrum, defined as $\frac{1}{2\pi}\int_{-\infty}^{\infty} S(\boldsymbol{r}_{\rm p},\omega)\,{\rm d}\omega$, incorporate material dispersion, and extend the framework to multiple emitters, thereby deepening our understanding of quantum optical phenomena in realistic nanophotonic devices.

Appendix A

A1. Relationship between coupling coefficient and modal volume

The modal volume V_λ for mode λ is defined as[40]

$$V_\lambda = \frac{\int_V \varepsilon(\boldsymbol{r})|\boldsymbol{E}_\lambda(\boldsymbol{r})|^2\,{\rm d}^3\boldsymbol{r}}{\max\left[\varepsilon(\boldsymbol{r})|\boldsymbol{E}_\lambda(\boldsymbol{r})|^2\right]}.$$

If the modal field $\boldsymbol{E}_\lambda(\boldsymbol{r})$ is normalized and the QE is positioned at the maximum of $\varepsilon(\boldsymbol{r})|\boldsymbol{E}_\lambda(\boldsymbol{r})|^2$, then we have $V_\lambda = \frac{1}{\varepsilon(\boldsymbol{r}_0)|\boldsymbol{E}_\lambda(\boldsymbol{r}_0)|^2}$. Consequently, the coupling coefficient g_λ can be expressed as

$$\begin{aligned} g_\lambda &= -{\rm i}\omega_0(2\varepsilon_0\hbar\omega_\lambda)^{-1/2} d_0|\boldsymbol{E}_\lambda(\boldsymbol{r}_0)|\cos\theta \\ &= -{\rm i}\omega_0[2\varepsilon_0\hbar\omega_\lambda\varepsilon(\boldsymbol{r}_0)V_\lambda]^{-1/2} d_0\cos\theta, \end{aligned} \tag{A1}$$

where θ is the angle between $\boldsymbol{d}_0$ and $\boldsymbol{E}_\lambda(\boldsymbol{r}_0)$.

A2. Connecting the CMT Hamiltonian to Eq. (1)

CMT describes a dielectric system's properties based on individual subsystems and their interactions. For a two-subsystem example, each with a single resonant mode, the Hamiltonian is[41]

$$H_{\rm EM} = \hbar\omega b_1^\dagger b_1 + \hbar\omega b_2^\dagger b_2 + \hbar s b_1^\dagger b_2 + \hbar s^* b_1 b_2^\dagger, \tag{A2}$$

where b_1 ($b_1^\dagger$) and b_2 ($b_2^\dagger$) represent the photon annihilation (creation) operators for each subsystem's mode, ω is the resonant frequency and s is the coupling coefficient. Using the transformation

$$\begin{aligned} a_1 &= -\frac{1}{\sqrt{2}}\left(\frac{|s|}{s}b_1 - b_2\right), \\ a_2 &= \frac{1}{\sqrt{2}}\left(\frac{|s|}{s}b_1 + b_2\right) \end{aligned} \tag{A3}$$

and commutation relations $[b_i, b_j] = 0$, $\left[b_i, b_j^\dagger\right] = \delta_{ij}$, we get $[a_i, a_j] = 0$ and $\left[a_i, a_j^\dagger\right] = \delta_{ij}$. This diagonalizes the Hamiltonian into independent dressed states

$$H_{\mathrm{EM}} = \hbar\omega_1 a_1^\dagger a_1 + \hbar\omega_2 a_2^\dagger a_2, \tag{A4}$$

with $\omega_1 = \omega - |s|$ and $\omega_2 = \omega + |s|$. Extending Eq. (A4) to multiple non-resonant subsystems and adding a two-level QE, we arrive at the Hamiltonian in Eq. (1).

A3. Linking $\rho_S(\omega)$ to $\Gamma_S(\omega)$

To verify Eq. (8), substitute

$$g_\lambda = -\mathrm{i}\omega_0 \left(2\varepsilon_0\hbar\omega_\lambda\right)^{-1/2} \boldsymbol{E}_\lambda(\boldsymbol{r}_0)\cdot\boldsymbol{d}_0$$

into Eq. (7), yielding

$$\Gamma_S(\omega) = \frac{\pi d_0^2\omega_0^2}{\varepsilon_0\hbar\omega}\sum_{\lambda\in S}\left|\boldsymbol{E}_\lambda(\boldsymbol{r}_0)\cdot\hat{d}_0\right|^2\delta(\omega-\omega_\lambda). \tag{A5}$$

Combining with Eq. (6), we obtain

$$\Gamma_S(\omega) = \frac{\pi d_0^2\omega_0^2}{\varepsilon_0\hbar\omega}\rho_S(\omega). \tag{A6}$$

In vacuum, the spontaneous emission rate of a QE is[29]

$$\Gamma_0 = \frac{\omega_0^3 d_0^2}{3\pi\hbar\varepsilon_0 c^3}. \tag{A7}$$

The PLDOS in vacuum is[29]

$$\rho_0(\omega) = \frac{\omega^2}{3\pi^2c^3}. \tag{A8}$$

Combining Eqs. (A6)–(A8), along with $M_S(\omega) = \rho_S(\omega)/\rho_0(\omega)$, equation (8) can be verified.

A4. Linking $M_S(\omega)$ to radiated power

Previous work shows that for a dipole at position $\boldsymbol{r}_0$ with dipole moment $\boldsymbol{d}(t) = \mu\exp(-\mathrm{i}\omega t)\hat{d}_0$, its radiated power is[42]

$$P(\omega) = \frac{1}{4}\pi\mu^2\omega^2\sum_\lambda\left|\boldsymbol{E}_\lambda(\boldsymbol{r}_0)\cdot\hat{d}_0\right|^2\delta(\omega-\omega_\lambda), \tag{A9}$$

which indicates that each mode λ contributes independently to the total radiated power. Thus, restricting the summation over λ to the mode set S yields the dipole's radiated power of this mode set, i.e.,

$$P_S(\omega) = \frac{1}{4}\pi\mu^2\omega^2\sum_{\lambda\in S}\left|\boldsymbol{E}_\lambda(\boldsymbol{r}_0)\cdot\hat{d}_0\right|^2\delta(\omega-\omega_\lambda). \tag{A10}$$

Combining with Eq. (6), we get

$$P_S(\omega) = \frac{1}{4}\pi\mu^2\omega^2\rho_S(\omega). \tag{A11}$$

Applying this equation to the case of vacuum and taking S as the universal set S_{all}, we get

$$P_0(\omega) = \frac{1}{4}\pi\mu^2\omega^2\rho_0(\omega), \tag{A12}$$

where $P_0(\omega)$ is the dipole's radiated power in vacuum. From Eqs. (A11) and (A12), along with $M_S(\omega) = \rho_S(\omega)/\rho_0(\omega)$, we obtain

$$M_S(\omega) = \frac{P_S(\omega)}{P_0(\omega)}, \tag{A13}$$

which reduces the calculation of modal M factor to that of classical radiated power.

A5. Power spectrum: A green's function representation

The power spectrum can be equivalently expressed as[30,31]

$$S(\boldsymbol{r}_{\mathrm{p}},\omega) = \frac{\omega^2}{\varepsilon_0c^2}\left|\boldsymbol{G}(\boldsymbol{r}_{\mathrm{p}},\boldsymbol{r}_0,\omega)\cdot\boldsymbol{d}_0\right|\left\langle\sigma_-^\dagger(\omega)\,\sigma_-(\omega)\right\rangle, \tag{A14}$$

where $\boldsymbol{G}(\boldsymbol{r}_{\mathrm{p}},\boldsymbol{r}_0,\omega)$ represents the dyadic Green's function, connecting a source at $\boldsymbol{r}_0$ to a field point at $\boldsymbol{r}_{\mathrm{p}}$. $\sigma_-(\omega) = \int_0^\infty\sigma_-(t)\,\mathrm{e}^{\mathrm{i}\omega t}\,\mathrm{d}t$ is the local dipole or polarization spectrum in the Heisenberg picture. To transform Eq. (A14) into the Schrödinger picture, we write

$$\begin{aligned} \sigma_-(t)\left|\Psi(0)\right\rangle &= \mathrm{e}^{\frac{\mathrm{i}}{\hbar}tH}\sigma_-\,\mathrm{e}^{-\frac{\mathrm{i}}{\hbar}tH}\left|\Psi(0)\right\rangle \\ &= \mathrm{e}^{\frac{\mathrm{i}}{\hbar}tH}\sigma_-\left|\Psi(t)\right\rangle \\ &= C_e(t)\,\mathrm{e}^{\frac{\mathrm{i}}{\hbar}tH}\left|g,\{0\}\right\rangle \\ &= C_e(t)\left|g,\{0\}\right\rangle. \end{aligned} \tag{A15}$$

Consequently, we can express $\left\langle\sigma_-^\dagger(\omega)\,\sigma_-(\omega)\right\rangle$ as

$$\begin{aligned} &\left\langle\sigma_-^\dagger(\omega)\,\sigma_-(\omega)\right\rangle \\ &= \int_0^\infty\left\langle\Psi(0)\right|\sigma_-^\dagger(t_2)\,\mathrm{e}^{-\mathrm{i}\omega t_2}\,\mathrm{d}t_2\int_0^\infty\sigma_-(t_1)\left|\Psi(0)\right\rangle\mathrm{e}^{\mathrm{i}\omega t_1}\,\mathrm{d}t_1 \\ &= \left|\int_0^\infty C_e(t)\,\mathrm{e}^{\mathrm{i}\omega t}\,\mathrm{d}t\right|^2 \\ &= \left|\bar{C}_e(\omega)\right|^2. \end{aligned} \tag{A16}$$

Substituting Eq. (A16) back into Eq. (A14), we arrive at the power spectrum expressed in the Schrödinger picture

$$S(\boldsymbol{r}_{\mathrm{p}},\omega) = \frac{\omega^2}{\varepsilon_0c^2}\left|\boldsymbol{G}(\boldsymbol{r}_{\mathrm{p}},\boldsymbol{r}_0,\omega)\cdot\boldsymbol{d}\right|\left|\bar{C}_e(\omega)\right|^2. \tag{A17}$$

A6. Tuning effective lifetime via dipole orientation

The coupling strength g_λ shown in Eq. (A1) is proportional to $d_0 \cos\theta$. Thus, we can define an effective dipole moment $\boldsymbol{d}_0'$ with magnitude $d_0' = d_0 \cos\theta$ aligned with $\boldsymbol{E}_\lambda(\boldsymbol{r}_0)$. This leads to an effective vacuum lifetime $\tau_{\rm vac}' = 3\pi\hbar\varepsilon_0 c^3/(\omega_0^3 d_0'^2) = \tau_{\rm vac}/\cos^2\theta$. Obviously, a QE with dipole moment d_0 or lifetime $\tau_{\rm vac}$ at angle θ to $\boldsymbol{E}_\lambda(\boldsymbol{r}_0)$ interacts identically to a QE with dipole moment d_0' or lifetime $\tau_{\rm vac}'$ aligned with $\boldsymbol{E}_\lambda(\boldsymbol{r}_0)$. The vacuum lifetime discussed in this paper can thus be interpreted as the effective lifetime $\tau_{\rm vac}'$. By varying θ, we can tune $\tau_{\rm vac}'$ from $\tau_{\rm vac}$ to infinity, effectively controlling the coupling strength, as demonstrated in previous studies.[43]

Acknowledgment

Project supported by the Basic and Applied Basic Research Project, Guangzhou Basic Research Plan (Grant No. 202201011444).

References

[1] Walther H, Varcoe B T H, Englert B G and Becker T 2006 *Rep. Prog. Phys.* **69** 1325
[2] Lodahl P, Mahmoodian S and Stobbe S 2015 *Rev. Mod. Phys.* **87** 347
[3] González-Tudela A, Reiserer A, García-Ripoll J J and García-Vidal F J 2024 *Nat. Rev. Phys.* **6** 166
[4] Lounis B and Orrit M 2005 *Rep. Prog. Phys.* **68** 1129
[5] Hennessy K, Badolato A, Winger M, Gerace D, Atatüre M, Gulde S, Fält S, Hu E L and Imamoğlu A 2007 *Nature* **445** 896
[6] Laucht A, Villas-Bôs J M, Stobbe S, Hauke N, Hofbauer F, Böhm G, Lodahl P, Amann M C, Kaniber M and Finley J J 2010 *Phys. Rev. B* **82** 075305
[7] Arcari M, Söllner I, Javadi A, Lindskov Hansen S, Mahmoodian S, Liu J, Thyrrestrup H, Lee E H, Song J D, Stobbe S and Lodahl P 2014 *Phys. Rev. Lett.* **113** 093603
[8] Törmä P and Barnes W L 2015 *Rep. Prog. Phys.* **78** 013901
[9] Dutta H S, Goyal A K, Srivastava V and Pal S 2016 *Photonics Nanostruct. Fundam. Appl.* **20** 41
[10] Senellart P, Solomon G and White A 2017 *Nat. Nanotechnol.* **12** 1026
[11] Dovzhenko D S, Ryabchuk S V, Rakovich Y P and Nabiev I R 2018 *Nanoscale* **10** 3589
[12] Bitton O, Gupta S N and Haran G 2019 *Nanophotonics* **8** 559
[13] Scarpelli L, Lang B, Masia F, Beggs D M, Muljarov E A, Young A B, Oulton R, Kamp M, Höfling S, Schneider C and Langbein W 2019 *Phys. Rev. B* **100** 035311
[14] Arakawa Y and Holmes M J 2020 *Appl. Phys. Rev.* **7** 021309
[15] Tiranov A, Angelopoulou V, van Diepen C J, Schrinski B, Sandberg O A D A, Wang Y, Midolo L, Scholz S, Wieck A D, Ludwig A, Sϕrensen A S and Lodahl P 2023 *Science* **379** 389
[16] Heindel T, Kim J H, Gregersen N, Rastelli A and Reitzenstein S 2023 *Adv. Opt. Photonics* **15** 613
[17] Luo W, Cao L, Shi Y, Wan L, Zhang H, Li S, Chen G, Li Y, Li S, Wang Y, Sun S, Karim M F, Cai H, Kwek L C and Liu A Q 2023 *Light Sci. Appl.* **12** 175
[18] Englund D, Shields B, Rivoire K, Hatami F, Vučković J, Park H and Lukin M D 2010 *Nano Lett.* **10** 3922
[19] Faraon A, Santori C, Huang Z, Acosta V M and Beausoleil R G 2012 *Phys. Rev. Lett.* **109** 033604
[20] Hausmann B J M, Shields B J, Quan Q, Chu Y, de Leon N P, Evans R, Burek M J, Zibrov A S, Markham M, Twitchen D J, Park H, Lukin M D and Loncăr M 2013 *Nano Lett.* **13** 5791
[21] Wu S, Buckley S, Schaibley J R, Feng L, Yan J, Mandrus D G, Hatami F, Yao W, Vučković J, Majumdar A and Xu X 2015 *Nature* **520** 69
[22] Pyatkov F, Fütterling V, Khasminskaya S, Flavel B S, Hennrich F, Kappes M M, Krupke R and Pernice W H P 2016 *Nat. Photonics* **10** 420
[23] Hwang M S, Kim H R, Kim K H, Jeong K Y, Park J S, Choi J H, Kang J H, Lee J M, Park W I, Song J H, Seo M K and Park H G 2017 *Nano Lett.* **17** 1892
[24] Ota Y, Moriya R, Yabuki N, Arai M, Kakuda M, Iwamoto S, Machida T and Arakawa Y 2017 *Appl. Phys. Lett.* **110** 223105
[25] Gopinath A, Miyazono E, Faraon A and Rothemund P W K 2016 *Nature* **535** 401
[26] Chen L H, Chen G, Liu R and Wang X H 2019 *Sci. China Phys. Mech. Astron.* **62** 974211
[27] Chen G, Liu J F, Liu R, Liu G, Chen Y, Chen Z and Wang X H 2020 *Phys. Rev. A* **101** 013828
[28] Liu J, Chen G, Li L, Liu R, Li W, Liu G, Wu F and Chen Y 2022 *Sci. Rep.* **12** 6901
[29] Scully M O and Zubairy M S 1997 *Quantum Optics* (Cambridge: Cambridge University Press)
[30] Hughes S and Yao P 2009 *Opt. Express* **17** 3322
[31] Yu Y C, Liu J F, Zhuo X L, Chen G, Jin C J and Wang X H 2013 *Opt. Express* **21** 23486
[32] Joannopoulos J D, Johnson S G, Winn J N and Meade R D 2008 *Photonic Crystals: Molding the Flow of Light*, 2nd edn. (Princeton University Press)
[33] Akahane Y, Asano T, Song B S and Noda S 2003 *Nature* **425** 944
[34] Minkov M and Savona V 2014 *Sci. Rep.* **4** 5124
[35] Benevides R, Santos F G S, Luiz G O, Wiederhecker G S and Alegre T P M 2017 *Sci. Rep.* **7** 2491
[36] Wang X H, Wang R, Gu B Y and Yang G Z 2002 *Phys. Rev. Lett.* **88** 093902
[37] Wang X H, Gu B Y, Wang R and Xu H Q 2003 *Phys. Rev. Lett.* **91** 113904
[38] Chen G, Yu Y C, Zhuo X L, Huang Y G, Jiang H, Liu J F, Jin C J and Wang X H 2013 *Phys. Rev. B* **87** 195138
[39] Sullivan D M 2013 *Electromagnetic Simulation Using the FDTD Method* 2nd Edn. (Wiley)
[40] Chen G, Liu J F, Jiang H, Zhuo X L, Yu Y C, Jin C and Wang X H 2013 *Nanoscale Res. Lett.* **8** 187
[41] Chak P, Iyer R, Aitchison J S and Sipe J E 2007 *Phys. Rev. E* **75** 016608
[42] Xu Y, Vučković J S, Lee R K, Painter O J, Scherer A and Yariv A 1999 *J. Opt. Soc. Am. B* **16** 465
[43] Chen G, Liu J F, Jiang H X, Liu G, Chen Y, Chen Z and Wang X H 2019 *J. Phys. B: At. Mol. Opt. Phys.* **52** 035503